### Title
Flat-band-induced itinerant ferromagnetism in RbCo2Se2




### Journal
Physical Review B, 103(16)

### ISSN
2469-9950



### Authors
Huang, Jianwei
Wang, Zhicai
Pang, Hongsheng
et al.



### Publication Date
2021-04-01

### DOI
10.1103/physrevb.103.165105

Peer reviewed

# Flatband-Induced Itinerant Ferromagnetism in $RbCo_2Se_2$

Jianwei Huang,[1] Zhicai Wang,[2] Hongsheng Pang,[2] Han Wu,[1] Huibo Cao,[3] Sung-Kwan Mo,[4] Avinash Rustagi,[5,6] A. F. Kemper,[5] Meng Wang,[7,8,*] Ming Yi,[1,8,†] and R. J. Birgeneau[8,9,‡]

[1]*Department of Physics and Astronomy, Rice University, Houston, TX 77005, USA*
[2]*School of the Gifted Young, University of Science and Technology of China, Hefei, Anhui 230026, China*
[3]*Neutron Scattering Division, Oak Ridge National Laboratory, Oak Ridge, Tennessee 37831, USA*
[4]*Advanced Light Source, Lawrence Berkeley National Lab, Berkeley, CA 94720, USA*
[5]*Department of Physics, North Carolina State University, Raleigh, NC 27695, USA*
[6]*School of Electrical and Computer Engineering, Purdue University, West Lafayette, IN 47907*
[7]*School of Physics, Sun Yat-Sen University, Guangzhou, Guangdong 510275, China*
[8]*Department of Physics, University of California, Berkeley, CA 94720, USA*
[9]*Materials Science Division, Lawrence Berkeley National Laboratory, Berkeley, California 94720, USA*

(Dated: March 12, 2021)

$ACo_2Se_2$ ($A$=K,Rb,Cs) is a homologue of the iron-based superconductor, $AFe_2Se_2$. From a comprehensive study of $RbCo_2Se_2$ via measurements of magnetization, transport, neutron diffraction, angle-resolved photoemission spectroscopy, and first-principle calculations, we identify a ferromagnetic order accompanied by an orbital-dependent spin-splitting of the electronic dispersions. Furthermore, we identify the ordered moment to be dominated by a $d_{x^2-y^2}$ flatband near the Fermi level, which exhibits the largest spin splitting across the ferromagnetic transition, suggesting an itinerant origin of the ferromagnetism. In the broader context of the iron-based superconductors, we find this $d_{x^2-y^2}$ flatband to be a common feature in the band structures of both iron-chalcogenides and iron-pnictides, accessible via heavy electron doping.

## I. INTRODUCTION

The parent compounds of most iron-based superconductors (FeSCs) are collinear antiferromagnetic (AFM) metals[1], with nearly compensated hole and electron Fermi pockets separated by the AFM wavevector[2]. Superconductivity emerges with the suppression of the AFM order[3]. In the intercalated iron chalcogenides, $A_xFe_{2-\delta}Se_2$ (A=K,Rb,Cs), parent compounds typically exhibit insulating behaviors with a variety of AFM orders[4,5]. By tuning the iron content, one can achieve iron vacancy-free superconducting phases in $A_xFe_2Se_2$ (A=K,Rb,Cs)[6], which exhibit large electron Fermi pockets near the Brillouin zone (BZ) corners.

$ACo_2Se_2$ (A=K,Rb,Cs) is an isostructural homologue of the vacancy-free superconducting $AFe_2Se_2$ phase with Fe substituted by Co[7], albeit with distinct physical properties. While $AFe_2Se_2$ is a superconductor with an AFM insulating parent phase[4–6], $ACo_2Se_2$ exhibits metallic magnetic ground states without superconductivity. In particular, $ACo_2Se_2$ consists of planar ferromagnetic (FM) sheets that are either aligned ($KCo_2Se_2$ and $RbCo_2Se_2$) or anti-aligned (A-type AFM in $CsCo_2Se_2$)[7–10]. Due to the metallicity, an itinerant nature has been proposed as the origin of the magnetism[8,11]. In such a scenario, band splitting into the spin-majority and spin-minority bands is expected[12–14]. However, while the low temperature electronic structure of $KCo_2Se_2$ has been measured[15], no direct observation of electronic reconstruction across the FM transition has been reported for this series of itinerant magnets.

Here we report the evolution of the electronic structure of $RbCo_2Se_2$ across the FM transition via angle-resolved photoemission spectroscopy (ARPES), together with characterization by magnetization, transport and neutron diffraction measurements. We identify a nearly flatband near the Fermi level ($E_F$) that exhibits the largest splitting in the FM phase. From first-principle calculations, we identify this band to be a $d_{x^2-y^2}$ flatband that contributes the most to the density of states at $E_F$ and therefore drives the itinerant FM in this material. Furthermore, in the larger context of the FeSCs, we find this $d_{x^2-y^2}$ flatband to be a common feature in the calculated band structures in both the FeSe-based and FeAs-based systems that is accessible via heavy electron-doping. Combining the phenomenology across the FeSC families, we point out a connection between the emergence of various symmetry-breaking phases to the common features in the low energy Fe 3d bands tunable via carrier doping.

## II. METHODS

Single crystals of $RbCo_2Se_2$ were grown by the self-flux method[9]. High purity Rb, Co and Se were used as the starting materials and prepared in the ratio of 1:2:2. Sample magnetization and resistivity were measured with commercial MPMS and PPMS. Neutron diffraction was carried out on the HB3A four-circle diffractometer at the High Flux Isotope Reactor, Oak Ridge National Laboratory with a neutron wavelength of $\lambda = 1.553$Å selected by a bent perfect Si-220 monochromator[16]. The nuclear and magnetic structures were refined with the FullProf suite[17], resulting in a refined stoichiometry of $Rb_{0.93}Co_{1.87}Se_2$, and lattice constants $a = 3.870$ Å and $c = 13.876$ Å. ARPES measurements were carried out at beamline 10.0.1 of the Advanced Light Source with a Sci-

enta R4000 hemispherical energy analyzer. The energy resolution was set as 12.5 meV and the angular resolution was set as 0.3°. The photon energy of the light was set at 45 eV in an *s*-polarization geometry where the polarization vector was perpendicular to the electron analyzer slit. The samples were cleaved in situ at 30 K and kept in ultra high vacuum with a base pressure better than 3 $\times$ $10^{-11}$ torr during measurements.

The electronic structure calculations were performed using density functional theory (DFT) via QUANTUM ESPRESSO[18,19] with plane wave scalar relativistic pseudopotentials. The exchange-correlation energy was described by the generalized gradient approximation in the scheme proposed by Perdew-Burke-Ernzerhof[20] with a wavefunction cutoff energy of 40 Ry. The BZ was sampled for integration according to the scheme proposed by Monkhorst-Pack[21] with a grid of 10 $\times$ 10 $\times$ 10 k-points. Experimentally determined lattice constants were used with the out-of-plane Se atomic locations determined from relaxing the system. Calculations were performed for both the non-magnetic and the FM case where the total magnetization per unit cell was constrained to match that of the experimental value.

## III. RESULTS

The crystal and magnetic structures of $RbCo_2Se_2$ are shown in Fig. 1a. The ordered magnetic moment is determined from neutron diffraction to be 0.60(4) $\mu_B$ per Co site aligned along the $a$ axis, consistent with previous reports[7,9]. Magnetization measurement with the magnetic field in the $ab$ plane identifies an onset of the FM order at $T_c = 83$ K (Fig. 1c). A hysteresis behavior confirming the FM ground state is observed at 2 K as a function of external field (Fig. 1d). A kink at $T_c$ can also be identified in the resistance measurement (Fig. 1e). Finally, the integrated counts at the (0,0,4) magnetic Bragg peak from our neutron diffraction measurements clearly confirm the FM transition at $T_c$ (Fig. 1f).

Having confirmed the FM transition, we present the measured electronic structure in the paramagnetic phase. At 150 K > $T_c$, the Fermi surfaces (FSs) of $RbCo_2Se_2$ exhibit one small electron pocket ($\gamma$) around the BZ center, Γ, and three electron pockets around the BZ corner, X (Fig. 2a). To show better contrast, we present the raw data in the upper half of the FS, and its 2D curvature images in the bottom half. We note that the $X_1$ and $X_2$ points as labeled are equivalent under $C_4$ rotational symmetry of the tetragonal crystal structure. However, the map intensity appears different here due to the usage of linear horizontal polarization, which probes the $d_{xz}$ and $d_{yz}$ orbitals differently due to photoemission matrix element effects[22]. A large electron pocket ($\alpha$) around $X_1$ is easy to discern (Fig. 2a). The presence of a second weaker inner electron band ($\beta$) is evident both from the FS images at $X_1$ as well as from the momentum-distribution curve (MDC) taken from $E_F$, which can be

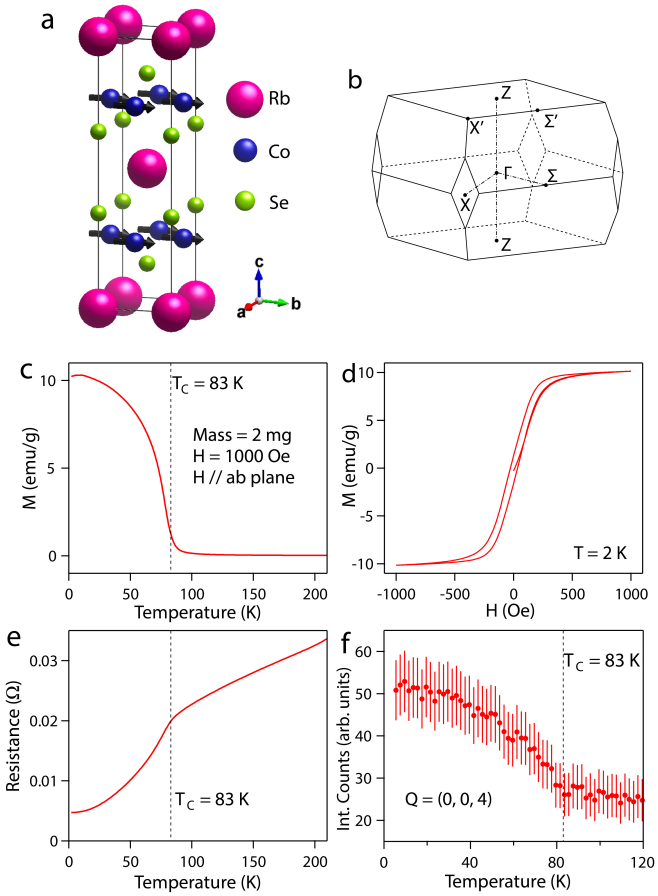


FIG. 1. **FM characterization.** (a) Crystal and magnetic structure of $RbCo_2Se_2$ with magnetic moments indicated by arrows. (b) BZ notations. (c) Temperature-dependent magnetization at 1000 Oe external magnetic field. (d) Field-dependent magnetization at 2 K. (e) Resistance as a function of temperature. (f) Neutron diffraction measurements of the integrated intensity of the (0,0,4) magnetic Bragg peak as a function of temperature.

fitted with four Lorentzian peaks on a constant background (Fig. 2b). A third electron band ($\varepsilon$) can be observed at the $X_2$ point due to the distinct matrix element effect for the two equivalent X-points (Fig. 1a)[22]. Its fitted $k_F$ points (Fermi momenta) are plotted in Fig. 2a, which are distinct from those of the $\alpha$ and $\beta$ electron bands, confirming a total of three electron pockets at the X point. The identification of their dominant orbital character and expected matrix element effects will be discussed in a later section. Compared with the iron-chalcogenide superconductors $AFe_2Se_2$, the electron pockets of $RbCo_2Se_2$ at the X point are much larger, consistent with additional electron doping provided by the substitution of Fe by Co[23,24].

In comparison, the number of FS sheets observed deep in the FM phase increases. Most notable is the splitting of the $\alpha$ FS at $X_1$ (Fig. 2c). This is evident both from the FS map in Fig. 2c and a comparison of the MDCs across $X_1$ (Fig. 2d), which can now be fitted with six

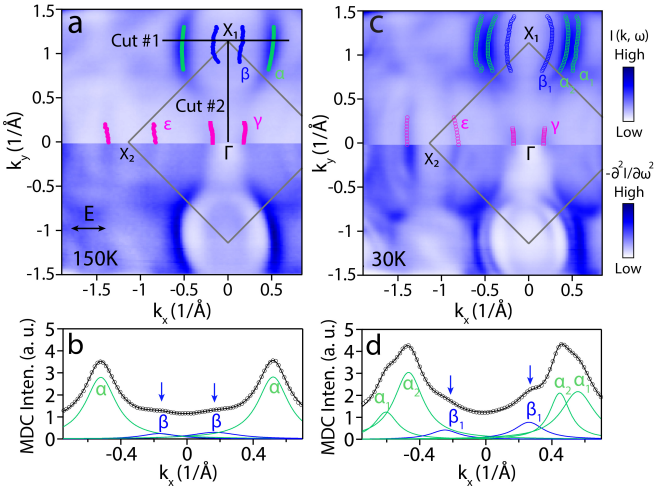


FIG. 2. **Fermi surfaces across $T_c$.** (a) FS mapping at 150 K $> T_c$. The $k_y > 0$ ($k_y < 0$) region shows the raw data (2D curvature). Markers indicate MDC-fitted FSs. (b) MDC at $E_F$ along cut #1 in (a) fitted with four Lorentzians and a constant background. The blue arrows indicate the $\beta$ band. (c,d) Same as (a,b) except taken at 30 K in the FM state.

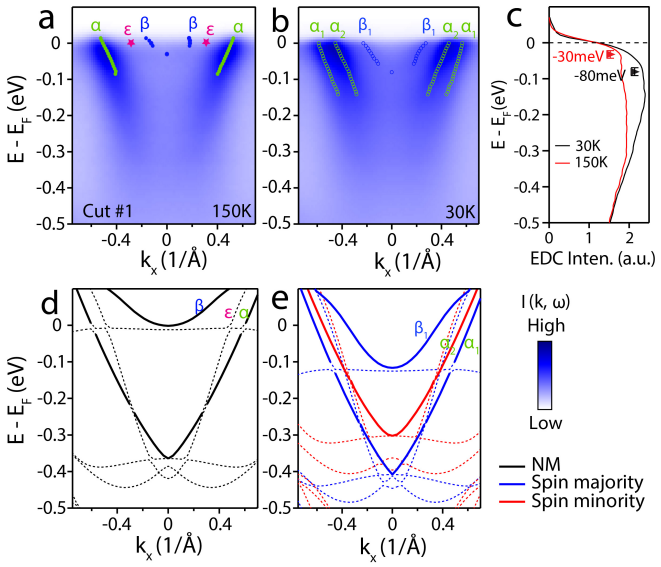


FIG. 3. **Electronic structure across $T_c$.** (a) Spectral image along cut #1 in Fig. 2a with MDC-fitted dispersions. The $k_F$ value of $\varepsilon$ is obtained from fitting the MDC at the equivalent $X_2$-point. (b) Same as (a) except taken at 30 K in the FM state. (c) Energy distribution curves (EDCs) at the $X_1$ point. The markers indicate the $\beta$ band bottom obtained by fitting the corresponding data points in (a) and (b) with a parabolic curve. Fitting uncertainty gives a $\pm$10 meV error bar. (d) DFT band calculations in the paramagnetic phase renormalized by a factor of 2.9. (e) Same as (d) except in the FM state.

Lorentzian peaks showing a splitting of the peak previously identified as the $\alpha$ pocket at 150 K. This is consistent with a band splitting due to the FM ordering. We therefore label these as the $\alpha_1$ and $\alpha_2$ pockets, which correspond to the spin-majority and spin-minority bands, respectively. The $k_F$ opening (defined by the separation in momentum) of the pair of peaks labeled $\beta_1$ has expanded compared to that of the $\beta$ pocket in the paramagnetic phase, suggesting that the pair observed at 30 K is likely the spin-majority branch of the $\beta$ band that has shifted downwards in energy while the spin minority $\beta_2$ band has shifted to above $E_F$ and hence is not observed. In contrast, we do not observe obvious shifts of the electron pocket ($\gamma$) at $\Gamma$ and the electron pocket ($\varepsilon$) at $X_2$ below $T_c$(Fig. 2a, b).

The spin-splitting of bands in the presence of the FM order can be further visualized from the band dispersions. Band images measured across $X_1$ in the paramagnetic phase (150 K) are shown in Fig. 3a. Related band dispersions obtained by MDC fitting as well as the $k_F$ positions of the $\varepsilon$ electron pocket are overlaid on the image. To understand better the observed bands, we have performed DFT calculations of non-magnetic and FM states of $RbCo_2Se_2$. Focusing around the X point in the paramagnetic phase (Fig. 3d), our observed dispersions show reasonable comparison with the calculated electron bands, where a total of 3 electron bands appear near $E_F$. From the size of the $k_F$ openings, the outermost band and the innermost band (solid black bands) likely correspond to the $\alpha$ and $\beta$ bands observed at $X_1$, while the middle band (dotted black band) correspond to the $\varepsilon$ band observed at $X_2$ (Fig. 2a). This assignment is further supported by a consideration of the orbital characters of these bands and the photoemission matrix element effects as will be discussed shortly. To match with the Fermi velocity of the outer-most $\alpha$ band, a renormalization factor of 2.9 is applied to the DFT calculations, suggesting moderate electronic correlations in $RbCo_2Se_2$. We also note that there exists an orbital-dependent relative shift that would be needed to match the calculations. Such behavior has been commonly observed in iron-based superconductors.[25–27]

In the FM state (Fig. 3b), the $\alpha$ band is observed to split into two bands, i.e. $\alpha_1$ and $\alpha_2$. The $\beta$ band is observed to shift down in energy compared to that in the paramagnetic phase. In the calculated band structure in the FM state (Fig. 3e), the $\alpha$ band splits into the spin majority band and spin minority band, marked by solid blue and red curves. Similarly, the $\beta$ band also splits with the spin majority band shifted down while the spin minority band has shifted to well above $E_F$. The bottom of the $\beta$ band is observed to be at 30 meV below $E_F$ in the paramagnetic state while the spin majority band is shifted down to 80 meV below $E_F$ in the FM state (Fig. 3c). An estimation based on the assumption of equal spin-splitting therefore locates the spin minority band of $\beta$ to be at 20 meV above $E_F$, and hence not observed.

Furthermore, we observe a nearly flat band from the spectra image at cut #2 along the $\Gamma$-X direction (Fig. 4a). The flat band sits close to $E_F$ at 150 K in the paramag-

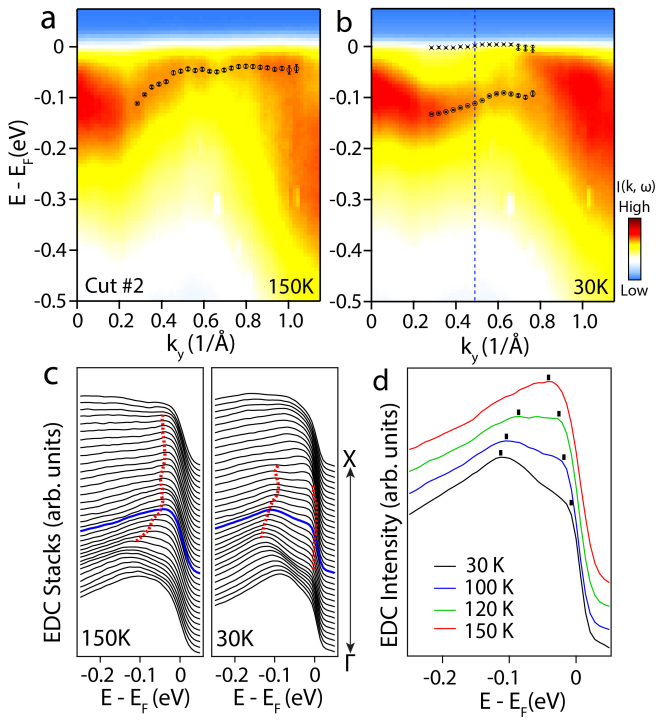


FIG. 4. **Flat band across $T_c$.** (a,b) Spectra images along cut #2 in Fig. 2a at 150 and 30 K, respectively. Markers are the corresponding fitted peak positions in (c). (c) EDC stacks of (a) and (b). Red markers indicated peak positions from fitting the EDCs with two Lorentzians and a constant background multiplied by the Fermi-Dirac function. (d) Temperature dependent EDCs at the momentum indicated by the blue dashed line in (b).

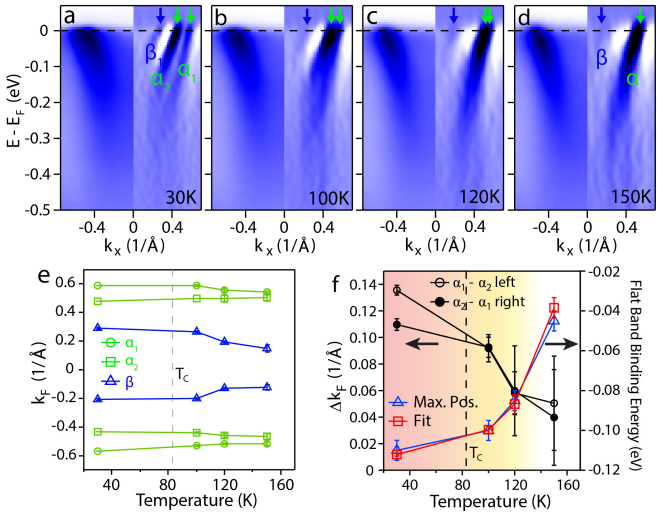


FIG. 5. **Temperature dependence of band splittings.** (a-d) Temperature-dependent spectra along cut #1 marked in Fig. 2a. The left (right) half shows the raw data (second momentum derivative). (e) Fitted $k_F$ of $\alpha_1$, $\alpha_2$ and $\beta_1$ bands as a function of temperature. Error bars are obtained from the fitting uncertainty. (f) Temperature dependence of $\alpha$ band $\Delta k_F$ and the shift of the flatband from fitting the peak position in the EDCs and maximum positions in Fig. 4d

netic state. It splits into two at 30 K in the FM state as is evident in the comparison of the EDC stacks between 30 K and 150 K where a single peak at 150 K splits into a peak at lower energy with a shoulder near $E_F$ at 30 K, which is likely the residual tail of the spin-minority band that has shifted to above $E_F$ (Fig. 4c). The band-splitting behavior of this flat band is reminiscent of that of the $\beta$ band where the spin-majority band is shifted down below $E_F$ while the spin-minority band shifts to above $E_F$. The diminishing of the flatband splitting with increasing temperature is shown by EDCs at different temperatures in Fig. 4d.

To confirm further the relation between the band splitting and the FM order, we examine the evolution of the spin splitting with temperature. With increasing temperature, the $\alpha_1$ and $\alpha_2$ bands are observed to merge (Fig. 5a-d). However, they remain split at 100 K. To quantify the splitting against temperature, we extract the $k_F$ of the $\alpha$ and $\beta$ bands by fitting the MDC at $E_F$ (Fig. 5e), from which we can also extract the $k_F$ differences (Fig. 5f). In addition, the splitting of the flatband can also be tracked from the peaks in the EDCs (Fig. 4d). This shows that while spin splitting of bands occurs across $T_c$, the onset of the splittings persists to a higher temperature than $T_c$, suggestive of ferromagnetic fluctuations in the paramagnetic state.

To understand better the behavior of the band-dependent splitting, we carried out orbital-projected DFT calculations of both non-magnetic and FM $RbCo_2Se_2$. From the nonmagnetic calculations, three electron bands appear around the X point (Fig. 6b), the relative sizes of which allow us to identify the observed $\alpha$, $\beta$ and $\varepsilon$ bands as the calculated bands with dominantly $d_{xz/yz}$, $d_{x^2-y^2}$ and $d_{xy}$ orbital characters, respectively. This assignment is consistent with the expected photoemission matrix element effects, where under the s-polarization used, the $\alpha$ ($d_{xz}/d_{yz}$) band shows strong intensity at the $X_1$ point due to its odd symmetry with respect to the Γ-X direction, while the $\varepsilon$ ($d_{xy}$) band exhibits observable but weaker intensity at the $X_2$ point due to switched parity under the glide mirror symmetry[28]. The innermost $\beta$ band is usually not observable in FeSC parent compounds due to its high kinetic energy, but is now observable due to the heavy electron-doping from Co. We find a qualitative match between the calculated and measured dispersions with a renormalization factor of 2.9 to match the Fermi velocity of the observed $\alpha$ band (Fig. 3a). We also note that the $\gamma$ band is a highly $k_z$-dispersive band where its band bottom is below $E_F$ near Z and rises to above $E_F$ near Γ. Since we do observe the $\gamma$ electron band at the BZ center, we are likely measuring near $k_z = \pi$. Importantly, a flatband appears at $E_F$ in the nonmagnetic calculation along Γ-X with dominant $d_{x^2-y^2}$ orbital character, consistent with our ARPES measurements (Fig. 4a). Such a flatband leads

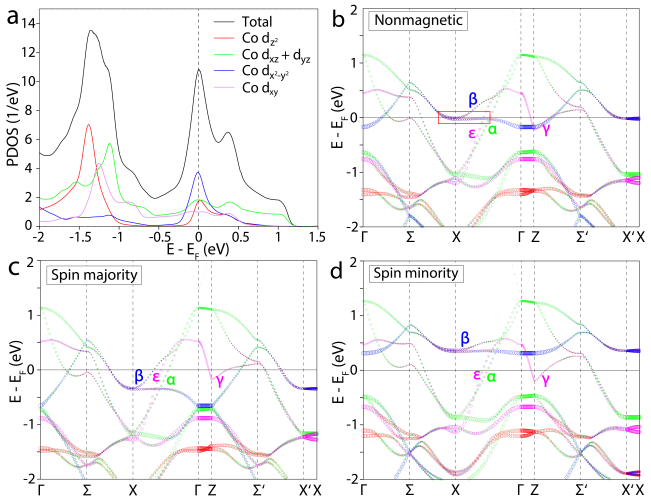


FIG. 6. **Calculated Electronic Structures.** (a) Calculated PDOS projected unto Co $d$ orbitals in the non-magnetic state. (b-d) Calculated orbital-resolved band dispersion in the non-magnetic, spin-majority, and spin-minority state, respectively. The marker size represents the spectral weight.

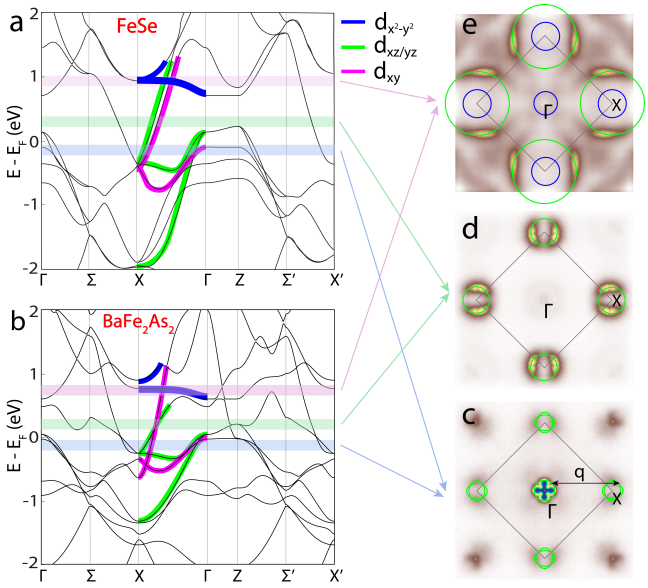


FIG. 7. **Electronic phases in iron-based superconductors.** (a,b) Band structure calculations of FeSe[30] and $BaFe_2As_2$[31]. Common features along Γ-X are highlighted by dominant orbitals. Horizontal lines represent different chemical potentials tunable via electron doping as exemplified by FSs of (c) Fe(Se,Te), (d) high $T_c$ $RbFe_2Se_2$, and (e) flatband itinerant FM $RbCo_2Se_2$.

to a large density of states (DOS) at $E_F$, which could induce a strong FS instability resulting in a band splitting - the spin majority band and minority band - to reduce the overall energy of the system[11,29].

Indeed, a large DOS at $E_F$ is contributed by this flatband as seen from the calculated orbital-projected DOS for the nonmagnetic phase (Fig. 6a). In the calculation for the FM state, the spin splitting between the majority and minority bands is orbital-dependent: largest in the $d_{x^2-y^2}$ flatband, followed by the $d_{xz/yz}$ bands, and finally the $d_{xy}$ bands (Fig. 6c and d). This is consistent with our ARPES measurements in that the splittings of the flatband and the $\alpha$ and $\beta$ bands are clearly observed while those of the $\varepsilon$ band are not. Similarly, the $\gamma$ electron band observed at Γ is also dominantly of $d_{xy}$ character, where no significant modification across $T_c$ is observed (Fig. 2a, c). We can confirm further the role of the $d_{x^2-y^2}$ flatband to the itinerant FM by calculating the contribution to the ordered moment from different orbitals (TABLE I). Indeed, the $d_{x^2-y^2}$ orbital contributes 0.3 $\mu_B$ out of the 0.60(4) $\mu_B$ total ordered magnetic moment per Co site (TABLE I) while the $d_{xy}$ orbital contributes merely 0.02 $\mu_B$. Our combined experimental and theoretical results are in support of a flatband-induced itinerant origin for the ferromagnetism in $RbCo_2Se_2$.

Finally, it is interesting to note that this $d_{x^2-y^2}$ flatband is a commonality in the electronic structure of FeSCs. Besides the $ACo_2Se_2$ family, $SrCo_2As_2$ has also been recently identified to host itinerant ferromagnetism due to a flatband near $E_F$[32,33]. Taking the observed electronic phases together amongst FeSCs, we point out the following phenomenology in relation to the common electronic structure of the Fe 3$d$ orbitals. We use band structure calculations for FeSe[30] and $BaFe_2As_2$[31] to represent the FeSe-based and FeAs-based materials where common features are highlighted (Fig. 7a and b). We illustrate three main types of fermiologies observed. For the undoped parent compounds such as $BaFe_2As_2$, NaFeAs, LaFeAsO, and Fe(Te,Se), the chemical potential leads to quasi-nested hole pockets at the BZ center and electron pockets at the BZ corner, where a collinear spin density wave appears at the nesting wavevector with the associated nematic order (Fig. 7c)[25,27,34–38]. Superconductivity appears when these competing orders are suppressed with doping or chemical pressure. With further heavy electron doping, the chemical potential shifts up (green line in Fig. 7a and b) such that the hole bands at Γ sink below $E_F$, leaving enlarged electron pockets at the BZ corner, largely destroying the nesting condition. The group of materials exhibiting this type of fermiology includes the heavily electron-doped iron-chalcogenides such as $AFe_2Se_2$[23,24,39], (Li,Fe)OHFeSe [40,41], and monolayer FeSe film grown on $SrTiO_3$ substrate[42–45], exhibiting no competing ordered ground states and superconductivity appears with $T_c$ of 30 K to 65 K. With further electron

TABLE I. Orbital-resolved contribution of the magnetic moment from the Co 3d orbitals, with a total of 0.60(4) $\mu_B$ per Co from all orbitals.

| Orbital | $d_{x^2-y^2}$ | $d_{xz/yz}$ | $d_{xy}$ | $d_{z^2}$ |
|---|---|---|---|---|
| Magnetic moment ($\mu_B$) | 0.30 | 0.10 | 0.02 | 0.11 |

doping, as achieved by replacing Fe with Co, the chemical potential can be tuned further up (pink line in Fig. 7a and b) where the electron pockets at the zone corner are further enlarged. In this doping regime, a flatband appears near $E_F$, as has been identified in both $SrCo_2As_2$ and $ACo_2Se_2$, driving the electronic system into an itinerant ferromagnetic state[15,33,46–48]. It is interesting to point out that optimal superconductivity amongst FeSCs appears in the heavily electron-doped iron-chalcogenides where the Fermiology is farthest away from instabilities leading to competing phases–on one side the quasi-nesting inductive of SDW order, and on the other the flatband inductive of itinerant ferromagnetism.

## IV. CONCLUSION

To summarize, we report the evolution of the electronic structure of the itinerant ferromagnetic compound $RbCo_2Se_2$ across its ferromagnetic transition. In the paramagnetic state, the much enlarged electron Fermi pockets around the BZ corner indicate the heavy electron doping from its superconducting isostructural analog $RbFe_2Se_2$. A renormalization factor of 2.9 suggests moderate electron-electron correlations, comparable with those in the iron-based superconductors. We find an orbital-dependent band splitting in the ferromagnetic state. In comparison to first-principle calculations, we find our observations to be consistent with a flatband itinerant origin of the ferromagnetism. Furthermore, the band splitting is observed to persist within a finite temperature window above the ferromagnetic transition, suggesting ferromagnetic fluctuations above the long range ordering temperature. Finally, we point out a phenomenological observation of the appearance of high temperature superconductivity in the iron-based superconductors bounded by competing phases of SDW and nematicity on one side in a quasi-nested Fermiology and flatband itinerant ferromagnetism on the other side, tunable via carrier doping.

## ACKNOWLEDGMENTS

This research used resources of the Advanced Light Source, a U.S. DOE Office of Science User Facility under contract no. DE-AC02-05CH11231, and the High-Flux Isotope Reactor, a DOE Office of Science User Facility operated by the Oak Ridge National Laboratory. The work at LBL was funded by the U.S. Department of Energy, Office of Science, Office of Basic Energy Sciences, Materials Sciences and Engineering Division under Contract No. DE-AC02-05-CH11231 (Quantum Materials program KC2202). The work at Rice University was supported by the Robert A. Welch Foundation Grant No. C-2024 as well as the Alfred P. Sloan Foundation. Work at Sun Yat-Sen University was supported by the National Natural Science Foundation of China (Grant No. 11904414), Natural Science Foundation of Guangdong (No. 2018A030313055), National Key Research and Development Program of China (No. 2019YFA0705700), and Young Zhujiang Scholar program. A.F.K. was supported by NSF DMR-1752713.

* wangmeng5@mail.sysu.edu.cn
† mingyi@rice.edu
‡ robertjb@berkeley.edu

[1] C. de la Cruz, Q. Huang, J. W. Lynn, J. Li, W. R. II, J. L. Zarestky, H. A. Mook, G. F. Chen, J. L. Luo, N. L. Wang, and P. Dai, Nature **453**, 899 (2008).
[2] M. Yi, Y. Zhang, Z.-X. Shen, and D. Lu, npj Quantum Materials **2**, 57 (2017).
[3] A. A. Kordyuk, Low Temperature Physics **38**, 888 (2012).
[4] P. Dai, Reviews of Modern Physics **87**, 855 (2015).
[5] M. Wang, M. Yi, H. Cao, C. de la Cruz, S. K. Mo, Q. Z. Huang, E. Bourret-Courchesne, P. Dai, D. H. Lee, Z. X. Shen, and R. J. Birgeneau, Physical Review B **92**, 121101 (2015).
[6] M. Wang, M. Yi, W. Tian, E. Bourret-Courchesne, and R. J. Birgeneau, Physical Review B **93**, 075155 (2016).
[7] G. Huan, M. Greenblatt, and M. Croft, Eur. J. Solid State Inorg. Chem. **26**, 193 (1989).
[8] G. Huan and M. Greenblatt, Journal of the Less-Common Metals **156**, 247 (1989).
[9] J. Yang, B. Chen, H. Wang, Q. Mao, M. Imai, K. Yoshimura, and M. Fang, Physical Review B **88**, 064406 (2013).
[10] F. von Rohr, A. Krzton-Maziopa, V. Pomjakushin, H. Grundmann, Z. Guguchia, W. Schnick, and A. Schilling, Journal of Physics: Condensed Matter **28**, 276001 (2016).
[11] E. C. Stoner, Proceedings of the Royal Society of London. Series A. Mathematical and Physical Sciences **165**, 372 (1938).
[12] H.-B. Yang, S.-C. Wang, A. K. P. Sekharan, H. Matsui, S. Souma, T. Sato, T. Takahashi, T. Takeuchi, J. C. Campuzano, R. Jin, B. C. Sales, D. Mandrus, Z. Wang, and H. Ding, Physical Review Letters **92**, 246403 (2004).
[13] M. Güttler, A. Generalov, M. M. Otrokov, K. Kummer, K. Kliemt, A. Fedorov, A. Chikina, S. Danzenbächer, S. Schulz, E. V. Chulkov, Y. M. Koroteev, N. Caroca-Canales, M. Shi, M. Radovic, C. Geibel, C. Laubschat, P. Dudin, T. K. Kim, M. Hoesch, C. Krellner, and D. V. Vyalikh, Scientific Reports **6**, 24254 (2016).
[14] F. Mazzola, V. Sunko, S. Khim, H. Rosner, P. Kushwaha, O. J. Clark, L. Bawden, I. Marković, T. K. Kim, M. Hoesch, A. P. Mackenzie, and P. D. C. King, Proceedings of the National Academy of Sciences **115**, 12956 (2018).
[15] Z. H. Liu, Y. G. Zhao, Y. Li, L. L. Jia, Y. P. Cai, S. Zhou, T. L. Xia, B. Büchner, S. V. Borisenko, and S. C. Wang,

Journal of Physics: Condensed Matter **27**, 295501 (2015).
[16] B. C. Chakoumakos, H. Cao, F. Ye, A. D. Stoica, M. Popovici, M. Sundaram, W. Zhou, J. S. Hicks, G. W. Lynn, and R. A. Riedel, Journal of Applied Crystallography **44**, 655 (2011).
[17] J. Rodríguez-Carvajal, Physica B: Condensed Matter **192**, 55 (1993).
[18] P. Giannozzi, S. Baroni, N. Bonini, M. Calandra, R. Car, C. Cavazzoni, D. Ceresoli, G. L. Chiarotti, M. Cococcioni, I. Dabo, A. Dal Corso, S. de Gironcoli, S. Fabris, G. Fratesi, R. Gebauer, U. Gerstmann, C. Gougoussis, A. Kokalj, M. Lazzeri, L. Martin-Samos, N. Marzari, F. Mauri, R. Mazzarello, S. Paolini, A. Pasquarello, L. Paulatto, C. Sbraccia, S. Scandolo, G. Sclauzero, A. P. Seitsonen, A. Smogunov, P. Umari, and R. M. Wentzcovitch, Journal of Physics: Condensed Matter **21**, 395502 (2009).
[19] P. Giannozzi, O. Andreussi, T. Brumme, O. Bunau, M. Buongiorno Nardelli, M. Calandra, R. Car, C. Cavazzoni, D. Ceresoli, M. Cococcioni, N. Colonna, I. Carnimeo, A. Dal Corso, S. De Gironcoli, P. Delugas, R. A. Distasio, A. Ferretti, A. Floris, G. Fratesi, G. Fugallo, R. Gebauer, U. Gerstmann, F. Giustino, T. Gorni, J. Jia, M. Kawamura, H. Y. Ko, A. Kokalj, E. Kücükbenli, M. Lazzeri, M. Marsili, N. Marzari, F. Mauri, N. L. Nguyen, H. V. Nguyen, A. Otero-De-La-Roza, L. Paulatto, S. Poncé, D. Rocca, R. Sabatini, B. Santra, M. Schlipf, A. P. Seitsonen, A. Smogunov, I. Timrov, T. Thonhauser, P. Umari, N. Vast, X. Wu, and S. Baroni, Journal of Physics Condensed Matter **29**, 465901 (2017).
[20] "We used the pseudopotentials Rb.pbe-sp-hgh.UPF, Co.pbe-nd-rrkjus.UPF, and Se.pbe-n-rrkjus_psl.0.2.UPF from the QUANTUM ESPRESSO pseudopotential data base: http://www.quantum-espresso.org/pseudopotentials,".
[21] H. J. Monkhorst and J. D. Pack, Physical Review B **13**, 5188 (1976).
[22] M. Yi, D. Lu, J.-H. Chu, J. G. Analytis, A. P. Sorini, A. F. Kemper, B. Moritz, S.-K. Mo, R. G. Moore, M. Hashimoto, W.-S. Lee, Z. Hussain, T. P. Devereaux, I. R. Fisher, and Z.-X. Shen, Proceedings of the National Academy of Sciences **108**, 6878 (2011).
[23] D. Mou, S. Liu, X. Jia, J. He, Y. Peng, L. Zhao, L. Yu, G. Liu, S. He, X. Dong, J. Zhang, H. Wang, C. Dong, M. Fang, X. Wang, Q. Peng, Z. Wang, S. Zhang, F. Yang, Z. Xu, C. Chen, and X. J. Zhou, Physical Review Letters **106**, 107001 (2011).
[24] Y. Zhang, L. X. Yang, M. Xu, Z. R. Ye, F. Chen, C. He, H. C. Xu, J. Jiang, B. P. Xie, J. J. Ying, X. F. Wang, X. H. Chen, J. P. Hu, M. Matsunami, S. Kimura, and D. L. Feng, Nature Materials **10**, 273 (2011).
[25] M. Yi, D. H. Lu, J. G. Analytis, J.-H. Chu, S.-K. Mo, R.-H. He, R. G. Moore, X. J. Zhou, G. F. Chen, J. L. Luo, N. L. Wang, Z. Hussain, D. J. Singh, I. R. Fisher, and Z.-X. Shen, Physical Review B **80**, 024515 (2009).
[26] V. Brouet, P.-H. Lin, Y. Texier, J. Bobroff, A. Taleb-Ibrahimi, P. Le Fèvre, F. Bertran, M. Casula, P. Werner, S. Biermann, F. Rullier-Albenque, A. Forget, and D. Colson, Physical Review Letters **110**, 167002 (2013).
[27] M. D. Watson, T. K. Kim, A. A. Haghighirad, N. R. Davies, A. McCollam, A. Narayanan, S. F. Blake, Y. L. Chen, S. Ghannadzadeh, A. J. Schofield, M. Hoesch, C. Meingast, T. Wolf, and A. I. Coldea, Physical Review B **91**, 155106 (2015).
[28] V. Brouet, M. F. Jensen, P.-H. Lin, A. Taleb-Ibrahimi, P. Le Fèvre, F. Bertran, C.-H. Lin, W. Ku, A. Forget, and D. Colson, Physical Review B **86**, 075123 (2012).
[29] S. Blundell and D. Thouless, American Journal of Physics **71**, 94 (2003).
[30] A. Subedi, L. Zhang, D. J. Singh, and M. H. Du, Physical Review B **78**, 134514 (2008).
[31] S. Graser, A. F. Kemper, T. A. Maier, H.-P. Cheng, P. J. Hirschfeld, and D. J. Scalapino, Physical Review B **81**, 214503 (2010).
[32] S. Shen, W. Zhong, D. Li, Z. Lin, Z. Wang, X. Gu, and S. Feng, Inorganic Chemistry Communications **103**, 25 (2019).
[33] Y. Li, Z. Yin, Z. Liu, W. Wang, Z. Xu, Y. Song, L. Tian, Y. Huang, D. Shen, D. L. Abernathy, J. L. Niedziela, R. A. Ewings, T. G. Perring, D. M. Pajerowski, M. Matsuda, P. Bourges, E. Mechthild, Y. Su, and P. Dai, Physical Review Letters **122**, 117204 (2019).
[34] J.-H. Chu, J. G. Analytis, K. De Greve, P. L. McMahon, Z. Islam, Y. Yamamoto, and I. R. Fisher, Science **329**, 824 (2010).
[35] J.-H. Chu, H.-H. Kuo, J. G. Analytis, and I. R. Fisher, Science **337**, 710 (2012).
[36] R. M. Fernandes, A. V. Chubukov, and J. Schmalian, Nature Physics **10**, 97 (2014).
[37] G. Liu, H. Liu, L. Zhao, W. Zhang, X. Jia, J. Meng, X. Dong, J. Zhang, G. F. Chen, G. Wang, Y. Zhou, Y. Zhu, X. Wang, Z. Xu, C. Chen, and X. J. Zhou, Physical Review B **80**, 134519 (2009).
[38] K. Nakayama, Y. Miyata, G. N. Phan, T. Sato, Y. Tanabe, T. Urata, K. Tanigaki, and T. Takahashi, Physical Review Letters **113**, 237001 (2014).
[39] T. Qian, X.-P. Wang, W.-C. Jin, P. Zhang, P. Richard, G. Xu, X. Dai, Z. Fang, J.-G. Guo, X.-L. Chen, and H. Ding, Physical Review Letters **106**, 187001 (2011).
[40] L. Zhao, A. Liang, D. Yuan, Y. Hu, D. Liu, J. Huang, S. He, B. Shen, Y. Xu, X. Liu, L. Yu, G. Liu, H. Zhou, Y. Huang, X. Dong, F. Zhou, K. Liu, Z. Lu, Z. Zhao, C. Chen, Z. Xu, and X. J. Zhou, Nature Communications **7**, 10608 (2016).
[41] X. H. Niu, R. Peng, H. C. Xu, Y. J. Yan, J. Jiang, D. F. Xu, T. L. Yu, Q. Song, Z. C. Huang, Y. X. Wang, B. P. Xie, X. F. Lu, N. Z. Wang, X. H. Chen, Z. Sun, and D. L. Feng, Physical Review B **92**, 060504 (2015).
[42] D. Liu, W. Zhang, D. Mou, J. He, Y.-B. Ou, Q.-Y. Wang, Z. Li, L. Wang, L. Zhao, S. He, Y. Peng, X. Liu, C. Chen, L. Yu, G. Liu, X. Dong, J. Zhang, C. Chen, Z. Xu, J. Hu, X. Chen, X. Ma, Q. Xue, and X. Zhou, Nature Communications **3**, 931 (2012).
[43] S. Tan, Y. Zhang, M. Xia, Z. Ye, F. Chen, X. Xie, R. Peng, D. Xu, Q. Fan, H. Xu, J. Jiang, T. Zhang, X. Lai, T. Xiang, J. Hu, B. Xie, and D. Feng, Nature Materials **12**, 634 (2013).
[44] J. J. Lee, F. T. Schmitt, R. G. Moore, S. Johnston, Y.-T. Cui, W. Li, M. Yi, Z. K. Liu, M. Hashimoto, Y. Zhang, D. H. Lu, T. P. Devereaux, D.-H. Lee, and Z.-X. Shen, Nature **515**, 245 (2014).
[45] Q. Song, T. L. Yu, X. Lou, B. P. Xie, H. C. Xu, C. H. P. Wen, Q. Yao, S. Y. Zhang, X. T. Zhu, J. D. Guo, R. Peng, and D. L. Feng, Nature Communications **10**, 758 (2019).
[46] V. Bannikov, I. Shein, and A. Ivanovskii, Physica B: Condensed Matter **407**, 271 (2012).
[47] D. G. Quirinale, V. K. Anand, M. G. Kim, A. Pandey, A. Huq, P. W. Stephens, T. W. Heitmann, A. Kreyssig,

R. J. McQueeney, D. C. Johnston, and A. I. Goldman, Physical Review B **88**, 174420 (2013).
[48] Y. Li, Z. Liu, Z. Xu, Y. Song, Y. Huang, D. Shen, N. Ma, A. Li, S. Chi, M. Frontzek, H. Cao, Q. Huang, W. Wang, Y. Xie, R. Zhang, Y. Rong, W. A. Shelton, D. P. Young, J. F. DiTusa, and P. Dai, Physical Review B **100**, 094446 (2019).